Composites Part B 234 (2022) 109730

Contents lists available at ScienceDirect

Composites Part B

journal homepage: www.elsevier.com/locate/compositesb

Ultrahigh cavitation erosion resistant metal-matrix composites with biomimetic hierarchical structure

Ye Tian [a,b,c,1], Rui Yang [a,b,d,1], Zhoupeng Gu [e,f,1], Hang Zhao [a], Xianqian Wu [e], Shahed Taghian Dehaghani [h], Hao Chen [d], Xiaomei Liu [a,b,g], Tonghu Xiao [c], André McDonald [h], Hua Li [a,b,g], Xiuyong Chen [a,b,g,*]

[a] Key Laboratory of Marine Materials and Related Technologies, Zhejiang Key Laboratory of Marine Materials and Protective Technologies, Ningbo Institute of Materials Technology and Engineering, Chinese Academy of Sciences, Ningbo, 315201, China
[b] Zhejiang Engineering Research Center for Biomedical Materials, Cixi Institute of Biomedical Engineering, Ningbo Institute of Materials Technology and Engineering, Chinese Academy of Sciences, Ningbo, 315201, China
[c] Faculty of Materials Science and Chemical Engineering, Ningbo University, Ningbo, 315211, Zhejiang, China
[d] Department of Mechanical, Materials and Manufacturing Engineering, University of Nottingham Ningbo China, 199 Taikang East Road, Ningbo, 315100, China
[e] Institute of Mechanics, Chinese Academy of Sciences, Beijing, 100190, China
[f] School of Engineering Science, University of Chinese Academy of Sciences, Beijing, 100049, China
[g] Center of Materials Science and Optoelectronics Engineering, University of Chinese Academy of Sciences, Beijing, 100049, China
[h] Department of Mechanical Engineering, University of Alberta, Edmonton, AB T6G 1H9, Canada

ARTICLE INFO

Keywords:
Metal-matrix composites (MMCs)
Microstructures
Damage tolerance
Cavitation erosion

ABSTRACT

Cavitation erosion significantly impairs the serviceability of hydroelectric turbines and causes tremendous economic loss. Therefore, the demand for materials with effective resistance to cavitation erosion is imperative. Here, a novel nickel (Ni)-tungsten carbide (WC) composite coating with biomimetic hierarchical structure (BHS) is proposed. The BHS imitates cuttlebone in microscale and abalone nacre in nanoscale. In microscale, a three-dimensional cross-linking eutectic network of Ni-WC sandwiches divides Ni matrix into many small cells, which effectively inhibits crack propagation to an individual cell, controlling the damage caused by cavitation erosion. In nanoscale, numerical modelling results further reveal that the Ni-WC sandwiches can reduce the tensile stress triggered by cavitation impact and dissipate the impact energy, giving rise to ultrahigh cavitation erosion resistance behaviour. The design of similar structures may promote the development of other metal-matrix composites, establishing new methods for developing material systems with advanced properties.

1. Introduction

Hydroelectric power has been considered one of the essential parts in achieving carbon neutrality. However, cavitation erosion commonly occurs in hydro-turbine components, such as blade, runner, and volute, resulting in compromised serviceability and extended downtime. Microjets and shock waves generated by the collapse of cavitation bubbles repeatedly impact the surface of the material, causing severe damage in hydrodynamic systems [1,2]. Apart from optimisation of the mechanical structure of hydrodynamic equipment [3], considerable efforts have been devoted to developing protective coatings to resist cavitation erosion in harsh environments. Among various protective coatings, metal-ceramic composite coatings have been considered one of the most promising materials and extensively applied to resist cavitation erosion. Metal-ceramic composite coatings exhibit exceptional strength, toughness, and impact resistance [4,5], which are extremely challenging to achieve simultaneously in pure ceramic or metallic coatings. However, the boundary adhesion between the metal-ceramic phases is usually insufficient. In most cases, failure of these metal-ceramic composite coatings during cavitation erosion is attributed to brittle detachment of the hard ceramic phases and erosion of the exposed metallic binder phases [6]. Furthermore, it is generally accepted that interfaces, such as

* Corresponding author. Key Laboratory of Marine Materials and Related Technologies, Zhejiang Key Laboratory of Marine Materials and Protective Technologies, Ningbo Institute of Materials Technology and Engineering, Chinese Academy of Sciences, Ningbo, 315201, China.
E-mail address: chenxiuyong@nimte.ac.cn (X. Chen).
[1] These authors contributed equally: Ye Tian, Rui Yang, Zhoupeng Gu.

https://doi.org/10.1016/j.compositesb.2022.109730
Received 3 December 2021; Received in revised form 6 February 2022; Accepted 8 February 2022
Available online 18 February 2022

grain boundaries and phase boundaries, are preferentially attacked by the repeated impact of microjets and shock waves during the collapse of cavitation bubbles (up to Gpa [7,8]), resulting in the generation of large craters and other material failure [9–11]. In addition, despite having good resistance to cavitation erosion, only the region covered by the hard ceramic particles can be effectively protected. Thus, enhancing the adhesion at the interfaces and expanding the surface area covered by hard ceramic phases are highly desirable for promoting resistance to cavitation erosion.

Introducing post-treatment to the coatings is commonly adopted to improve their cavitation erosion resistance [12,13]. Here we have introduced laser remelting to the cold-sprayed nickel (Ni)-tungsten carbide (WC) coatings to promote the bonding at the Ni-WC interface, as the molten Ni can wet the WC particles. More importantly, we intend to alter the microstructure of the cold-sprayed Ni-WC coating into the one that mimics the cuttlebone in microscale and the abalone nacre in nanoscale. For cuttlebone, its cellular structure offers unique mechanical and structural properties, providing a layer-by-layer fracture mechanism when subjected to compressive stress, for which considerable studies have been reported [14,15]. This, in turn, helps avoid fatal damage under attack, and many bio-inspired structures have been designed based on this property [16]. Such a damage-control strategy may be applied for combating cavitation erosion. For abalone nacre, the aragonite layers are bonded with very elastic proteins and polysaccharides, exhibiting sandwiched structural features that possess extraordinarily high toughness and strength [17–21]. Researchers found that the sandwiched structure of nacre can reflect stress waves and significantly dissipate mechanical energy [22–28], providing structures with superior impact resistance, which is highly demanded for cavitation-erosion resisting materials.

The newly constructed layers are developed in accordance with the bio-mimic hierarchical structure (BHS) as proposed in Fig. 1 (the design process of BHS is described in detail in Text S1, Fig. S1 and Fig. S2), where the eutectic Ni-WC provides the nacre-like sandwiched nanostructure and the eutectic Ni-WC network provides the cuttlebone-like microstructure. It is hypothesized that such BHS Ni-WC coatings would provide exceptional cavitation erosion resistance via four regimes: (i) energy absorption by the nacre-like sandwiched ceramic-metallic nanostructure; (ii) damage control by the cuttlebone-like cellular microstructure enclosed by sandwiched ceramic-metallic nanostructure; (iii) improved bond strength at the phase boundaries by the wetting between WC particles and molten Ni during laser remelting; and (iv) large protected area by shape transformation of WC from particles to lamella. We suppose the newly designed BHS would facilitate the development of ultra-*anti*-cavitation erosion materials.

2. Experiment methods

2.1. Coating preparation and laser-remelting

Low-pressure cold gas dynamic spraying (SST series P, CenterLine, Ltd., Canada) was used to pre-deposit Ni/WC composite powders onto the top surface of substrates. The feedstock powder was composed of 8 wt% Ni powder (SST-N5001, Centerline, Ltd., Canada) and 92 wt% WC powder (Sulzer Metco, USA) which were admixed manually. The Ni and the WC powders for cold spraying were amorphous, whose size distribution was 5–45 and 10–45 μm, respectively. The substrate material was 316L stainless steel (316L SS, Zechanglong Ltd., China), and the dimension of the substrate was 20 mm in diameter and 10 mm in thickness. Before the spraying, the substrates were blasted by number 24 alumina grit medium with 0.3–1.0 MPa compressed air for 1 min and then cleaned with acetone to promote adhesion. The spraying parameters were adopted from the previous work [29], and the thickness of the as-sprayed (AS) coatings was ~1 mm. The AS coatings were grounded by 120, 400, 800, 1200, and 2000-grit SiC paper, respectively. Then, the grounded coatings were remelted by a laser (YLS-2000, IPG Photonics, USA) with different power levels (BHS-a, BHS-b, and BHS-c for the coatings remelted at 300, 400, and 500 W, respectively), a spot size of 0.5 mm, and an overlapping ratio of 50% at a transverse speed of 200 mm/min in nitrogen gas. A schematic diagram demonstrating the laser path is given in Fig. S3, and each sample was only scanned for one pass.

The sintered Ni-WC coatings were fabricated using a spark plasma sintering device (HPD 25 SI, FCT Systeme GmbH, Germany). Before the sintering process, the substrates were sandblasted in the same way for preparing the cold sprayed samples. Then, the substrates were put into the mould and followed by the filling-in of the manually blended Ni-WC powder (75 vol% Ni and 25 vol% WC, supplied by Changsha Tianjiu Metallics Ltd., China). The Ni powder for sintering was spherical and had a size distribution of 2–5 μm. The WC powder had the same size distribution, but it was amorphous. During the sintering process, the temperature rose to 1200 °C in 50 °C/min at 30 MPa. Next, the temperature was held at 1200 °C for 5 min, and then the sample was cooled to room temperature. Finally, the spark plasma sintered (SPS) sample was grounded and remelted as per the cold-sprayed coatings by a 400 W laser (BHS-SPS for the laser-remelted SPS coating).

2.2. Microstructure characterisation

Scanning electron microscopy (SEM, Quanta FEG 250, FEI, USA), electron backscattered diffraction (EBSD, NordlysMax2, Oxford Instruments, UK), X-ray diffraction (XRD, D8 ADVANCE, Bruker,

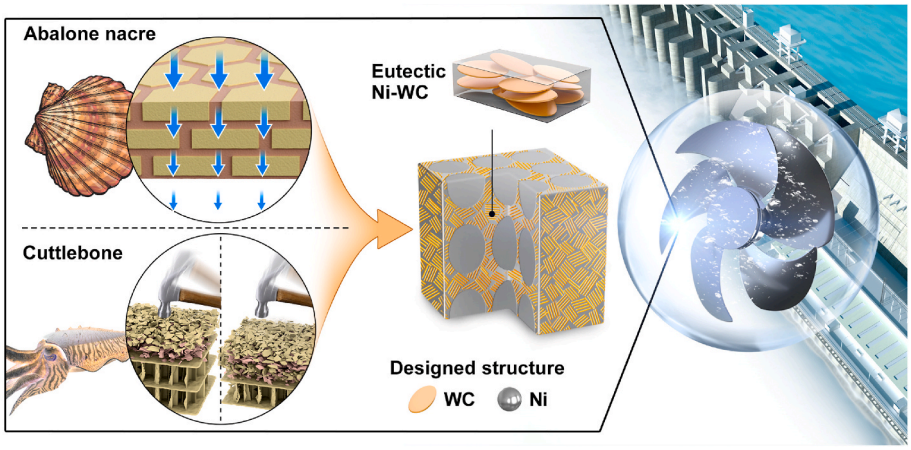

Fig. 1. Scheme of this work. This work intended to develop a microstructure to combine the features of abalone nacre and cuttlebone. A eutectic Ni-WC network formation within the treated coating is expected. The eutectic Ni-WC network provides a cell-by-cell fracture via mimicking the microstructure of cuttlebone and the eutectic region imitates the energy-dispersive function of abalone nacre.

Germany), and transmission electron microscopy (TEM, Talos F200x, ThemoFisher, USA) were used for characterisation of the BHS coatings. For the cross-section of the samples being characterized, the specimens were cut along the progressive path of the laser shown in Fig. S3. Before the SEM and XRD characterisation, the specimens were ground and then polished by 0.02 μm colloidal silica suspension.

Some as-remelted BHS coatings were chemically etched for SEM observation. The etchant was a mixture of 10 g of 37 wt% hydrochloric acid and 10 g of 35 wt% hydrogen peroxide solution (Shanghai Aladdin Biochemical Technology Ltd., China) in 30 ml of deionized water. The non-coated surface of the specimen was sealed by epoxy resin, and then the partially sealed specimen was submerged in the etchant for 5 min. Such a long duration of etching can ensure complete removal of Ni, and thus the microstructure formed by WC can be fully exposed. For the XRD detection, a copper anode with a curved graphite monochromator to filter K-beta wavelengths was used at 40 kV and 40 mA. The specimens were characterized using continuous XRD mod, where the 2θ diffraction angle was changed from 20° to 90° at a rate of 5° per minute. For the high-resolution TEM (HRTEM) characterisation, the specimens were thin films milled and cut from a polished cross-section of the sample by focused ion beam with liquid Ga^+ source (FIB, Auriga, Carl Zeiss, Germany).

2.3. Nano-indentation and Vickers hardness tests

Nano-indentation testing (Nano Indenter G200, MTS, USA) and Vickers hardness testing (Wilson VH3300, Buehler, Germany) were performed on the cross-sections of the samples. For the nano-indentation test, there were five random sites (40–50 μm beneath the surface) at the remelted region indented by a Berkovich diamond indenter for each tested sample. The maximum displacement into the surface was 2 μm at a strain rate of 0.01 μm/s. The indentation hardness (H_{IT}) and the indentation modulus (E_{IT}) were calculated using the software in the test rig. For the hardness test, five random locations (40–50 μm beneath the surface) in the remelted region were indented under a load of 0.2 kgf for each sample, and the average value of Vickers hardness was calculated by the software (DiaMet™) in the test rig. The tested samples were then characterized by SEM to observe the morphology of the indented sites.

2.4. Cavitation erosion test

Before the cavitation erosion testing, the surfaces of the samples were finished by 0.02 μm colloidal silica suspension, cleaned with acetone, and dried in a vacuum. The dried sample was then weighed by an analytical balance (Mettler 220, METTLER TOLEDO International Trading (Shanghai) Ltd., China). Next, the cavitation erosion properties of the samples were evaluated using ultrasonic vibratory apparatus (GBS-SCT 20A, Guobiao Ultrasonic Equipment Ltd., China) according to ASTM-G32-16, where the detailed parameters were described in our recent study [30]. Meanwhile, there were three samples tested for each type of the coating.

Each sample was exposed to cavitation erosion for 10 h, of which the mass loss was recorded every hour. Thus, the volume loss could be calculated by the quotient of the mass loss and the density of the material. The density of the AS coating, BHS coatings and the 316L SS substrate was measured by the buoyancy method, which was 10.53, 10.58 and 7.98 g/cm^3, respectively. After the cavitation erosion testing, the sample was characterized by a 3D profilometer (Up-Lambda 2, Rtec Instruments, USA) with white-light interferometry, investigating the surface roughness and the cavitation erosion crater. Three random regions with a dimension of 1.2 × 1.9 mm were investigated. The data were further analysed by MountainsMap® surface analysis software.

2.5. Numerical simulation

The dynamic compressive mechanical behaviours of the pure Ni structure and the laser-remelted Ni-WC structure were simulated by LS-DYNA [31] to analyse the cavitation impact resistant properties of the bioinspired interfaces. Figs. S4a–b shows the schematic diagram of the numerical simulation model of the pure Ni and the laser-remelted Ni-WC with 1000 × 200 × 750 nm^3 in the spatial dimensions. As shown in Fig. S4b, the regions of 100–150 nm and 250–300 nm below the loading surface represent WC, and the other is Ni. Both the pure Ni and the laser-remelted Ni-WC models were meshed with 960,000 elements. The size of the elements at 0–400 nm below the loading surface was 5 × 5 × 5 nm, and the size at 400–750 nm was 5 × 5 × 10 nm. A triangular shock wave with a peak value of 1 GPa and duration of 40 ps [32], as given in Fig. S4c, was applied on the upper surface of the models. The constitutive relationships of Ni and WC are shown in Fig. S4d, and the specific physical parameters of Ni and WC are given in Table S1.

3. Results

3.1. Microstructure of the biomimetic hierarchically structured coatings

The microstructure characterisations of the BHS-b coating are shown in Fig. 2. The SEM image of the molten pool (Fig. 2a) shows a uniform remelted zone. There are large WC grains at the edge of the molten pool, as highlighted by yellow arrows (which form segmentations as shown in Fig. S5). A magnified SEM image of the cross-section of the BHS-b coating is also given in Fig. 2a, showing the BHS-b coating with eutectic Ni-WC networks formed by Ni-WC sandwiched structures, where the bright regions are WC precipitates, and the dark regions refer to Ni binder. As a result, the designed BHS as proposed in Fig. 1 was achieved. In addition, the XRD spectra (Fig. 2b and Fig. S6) show that the composition of the BHS Ni-WC coatings only consisted of FCC Ni and HCP WC. The absence of the diffraction peaks of W_2C, Ni_4W, and other chemicals may be attributed to their low concentration. The composition of the BHS coatings was also verified by scanning transmission electron microscopy (STEM) equipped with energy-dispersive spectroscopy (STEM-EDS) (Fig. 2c), showing that limited W and C diffused into the nearby Ni matrix.

To investigate the three-dimensional microstructure of the eutectic Ni-WC, the as-remelted coatings were etched to remove the Ni. As shown in Fig. 2a, a series of ordered and uniformly sized cells are enwrapped by the WC skeleton (the etched surface of all the BHS coatings are shown in Fig. S7). The WC grains are mostly lamellae, and the networking structure is composed of the pile-up of numerous lamellar WC precipitates. To further identify the microstructure at the Ni-WC interfaces, TEM characterisation was carried out for the BHS-b coating. The STEM image (Fig. 3b) c clearly shows that the WC precipitates are embedded in the Ni matrix. Stacking faults were observed according to the HRTEM images (Fig. 3c–d). The magnified HRTEM images and the corresponding selected area electron diffraction (SAED) patterns (Fig. 2d) show that the precipitates and the matrix in the laser-remelted layer are HCP WC and FCC Ni, respectively, which is consistent with the XRD spectrum (Fig. 2b). It is noteworthy that there is a complexion of WC_x at the WC/Ni interface according to the sudden contrast change at the interface (Figs. 2d and Fig. 3c–d), which was also reported in WC-Co cemented carbides [33,34]. As shown in the magnified HRTEM image (Fig. 2d), 2–5 atomic layers in the complexion are distributed at the WC(0001)/Ni interface.

3.2. Mechanical properties

As cavitation erosion relies on surface mechanical properties of materials, nano-indentation and Vickers hardness tests were performed, and the results are given in Fig. 4 (the indented surfaces are shown in Fig. S8 and Fig. S9). The BHS-b coating took the heaviest load with the greatest strain recovery (Fig. 4a), indicating its capability of absorbing elastic deformation energy. This agrees well with the BHS-b coating exhibiting the highest H_{IT}^2/E_{IT} ratio (Table S2), representing the ability

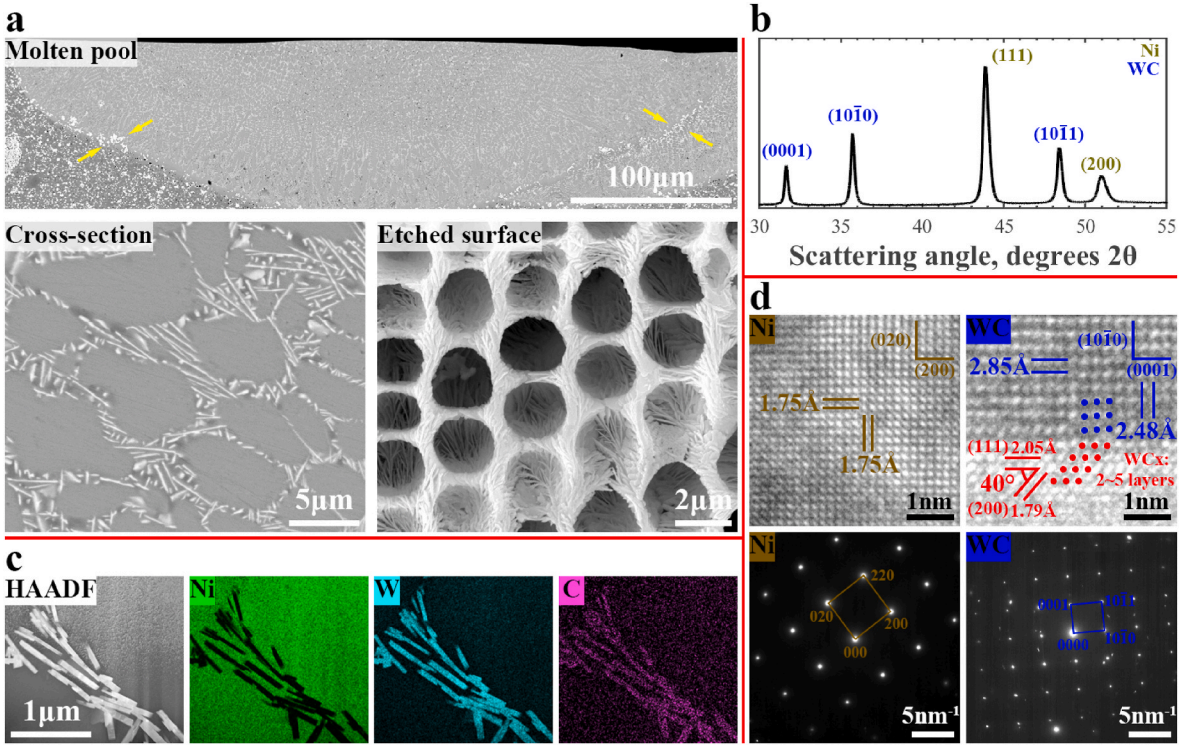

Fig. 2. Microstructural characteristics of the BHS-b coating.
a, SEM images showing the region with a single molten pool, polished cross-section, and etched surface. The width of the molten pool is ~500 μm, which is close to the diameter of the laser beam. Bands of large WC grains, as indicated by the yellow arrows, are observed at the edge of the molten pool, which are also observed in the other laser-remelted Ni-WC coatings (shown in Fig. S5). **b**, XRD spectrum of the laser-remelted coating, identified all the peaks as Ni and WC phases. The spectra of the other coatings were given in Fig. S6 **c**, TEM-EDX mappings of the coating. **d**, HRTEM images (sectioned from Fig. 3c–d) and SAED patterns of the coating, where complexions formed by layers of WC_x at the interface between Ni and WC grains. (For interpretation of the references to colour in this figure legend, the reader is referred to the Web version of this article.)

to absorb elastic deformation energy. The BHS-b coating also has the largest area enclosed by the load-displacement curve and the X-axis (Fig. 4a), suggesting that the BHS-b coating absorbed the greatest plastic deformation energy (among all the samples shown in Fig. S10). Furthermore, the largest H_{IT}/E_{IT} ratio, which indicates the resistance to contact damage caused by stress pulse attack, was also achieved by BHS-b coating (Table S2). As for the Vickers hardness (Fig. 4b), the BHS-b coating exhibited a value of 441 Hv, and the AS coating showed a value of 406 Hv. The augmented hardness of the BHS-b coating could be attributed to the good bonding between Ni and WC phases by the wetting during the laser remelting process. In addition, the network formed by the Ni-WC sandwich structure at the interfaces could also contribute to the augmented hardness.

3.3. Ultrahigh cavitation erosion resistance of the biomimetic coatings

The rate of volume loss ($\dot{V}_{loss}$) of stainless steel 316L (316L SS) and the BHS-b coatings subjected to cavitation erosion is shown in Fig. 5a (the data of cumulative volume loss (V_{loss}) and rate of volume loss ($\dot{V}_{loss}$) of all the samples are given in Table S3 and Table S4). The BHS coatings exhibited lower volume losses and erosion rates compared with the AS coating and 316L SS. The lowest volume loss at the 10th hour was achieved by the BHS-b coating, which was only 7% and 33% that of the AS coating and 316L SS, respectively. In addition, the $\dot{V}_{loss}$ of all the samples became stable after exposure to cavitation erosion for 7 h, and the average $\dot{V}_{loss}$ (after the 7th hour) of the BHS-b coating is 9% and 30% that of the AS coating and 316L SS substrate, respectively, indicating the excellent resistance to cavitation erosion of the BHS-b coating.

To further assess the anti-cavitation performances of the coatings, relative cavitation erosion resistance (R_c) versus microhardness of the Ni-WC coatings were summarized, and a comparison (Fig. 5b) was made with other reported engineering materials [10,35–48]. The detailed description about R_c is given in Fig. S11. As shown in Fig. 5b, the R_c of the BHS coating (17.8, BHS-CS in the figure) is much higher than that of the other engineering materials. As restricted by the cold-spraying technique, the distribution of WC particles in the AS coating is not homogeneous (about 25 ± 5% in volume). Thus, spark plasma sintering (SPS) was used to prepare the coatings with uniformly distributed WC particles and a fixed content (25 vol%) of WC (detailed data for the cumulative volume loss and the erosion rate are given in Table S3 and Table S4). As shown in Fig. 5b, the laser-remelted SPS Ni-WC sample (BHS-SPS in the figure) exhibits extremely superior resistance to cavitation erosion. The R_c value of the BHS-SPS coating is 56.6, which is approximately 27 and 23 times that of the AISI 316 stainless steel and nickel aluminium bronze (typical engineering alloys for cavitation erosion resistant applications), respectively. The superior cavitation erosion resistance of the BHS-SPS might be attributed to the even less defects and more homogeneous distribution of the Ni-WC eutectic network compared with the other BHS coatings (Fig. S12). Despite the dramatic increase in R_c, the microhardness of the BHS-SPS coating (<450 Hv) remains unchanged compared to that of the BHS coatings, indicating that the microhardness is not the only factor that influences the resistance to cavitation erosion. For typical engineering alloys, apart from 16Cr–5Ni with a R_c of 6.4, the others have the R_c of less than 5. Studies showed that grain boundaries and phase boundaries in alloys tend to be preferentially attacked by cavitation impact, resulting in poor resistance to cavitation erosion [9,10,43,49–51]. Typical engineering ceramics usually have extremely high hardness (>1000 Hv) but do not present outstanding resistance to cavitation erosion (R_c varies from 1.6 to 7.7). This is possibly attributed to their brittleness and inability to

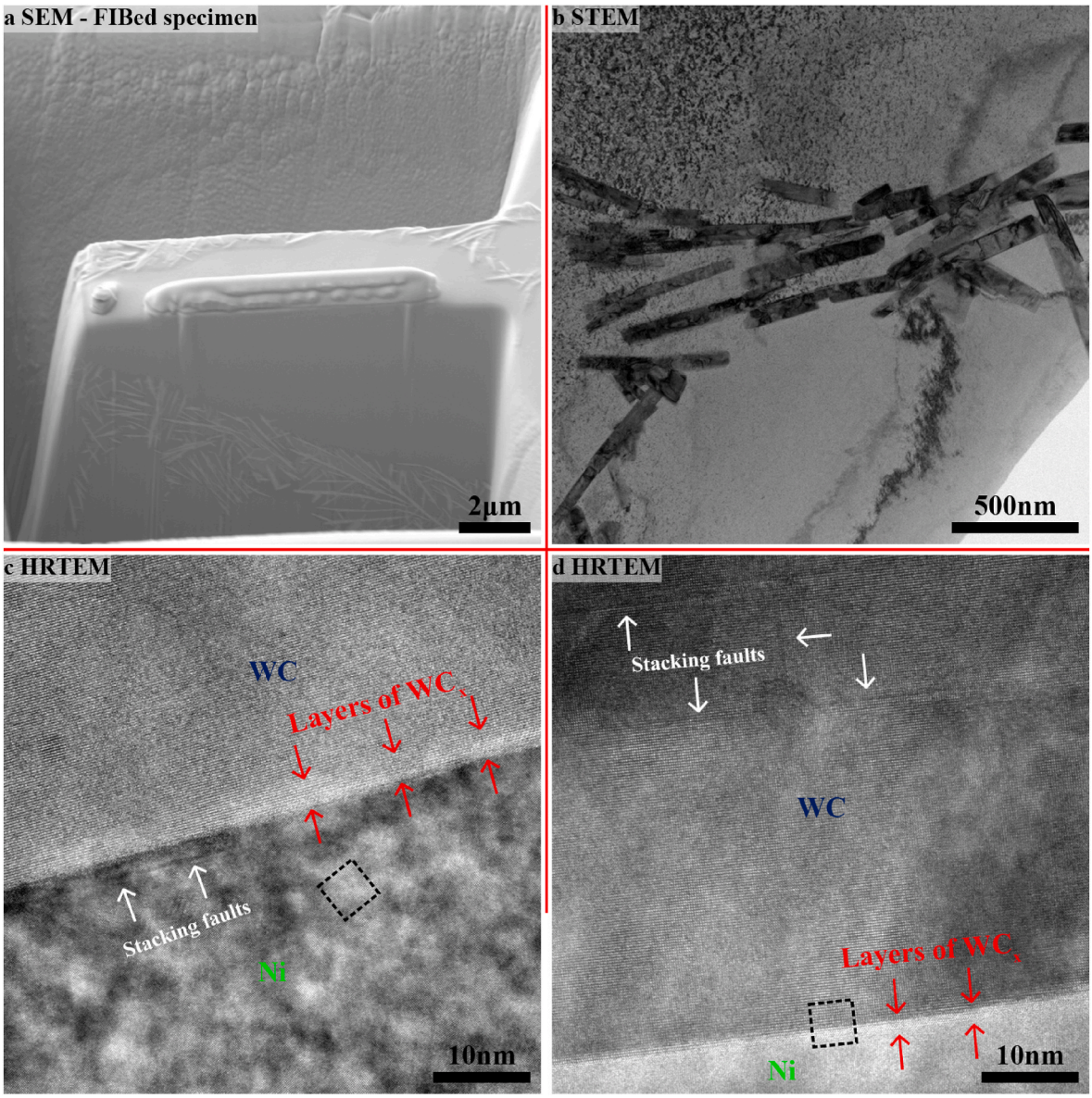

Fig. 3. TEM characterisation of the BHS-b coating.
a, SEM image of the specimen being cut by the focused ion beam. **b**, STEM image of the specimen. **c**-**d**, HRTEM images of the specimen, where the squared regions enclosed by black dashes correspond to the magnified HRTEM images in Fig. 2d. Complexions and stacking faults were observed, which are highlighted by red and white arrows. (For interpretation of the references to colour in this figure legend, the reader is referred to the Web version of this article.)

inhibit crack propagation during cavitation erosion. For typical engineering coatings, the microhardness varies from 600 to 1500 Hv, and their R_c value range is quite broad, ranging from 0.2 to 12.8. It is worth noting that although the microhardness of the BHS coatings in this work is much lower than that of typical engineering coatings and ceramics, ultrahigh cavitation erosion resistance was achieved, possibly attributed to the unique bio-mimic hierarchical structure.

The morphological changes of the AS and BHS-b coatings exposed to cavitation erosion are presented in Fig. 6 (the others are shown in Fig. S13). The cavitation craters and the exposed WC particles are seen in the AS coating (Fig. 6a&c). The profile of the crater is smooth, indicating the removal of a WC particle by cavitation erosion (Fig. 6a). The profile of the crater is smooth, indicating the removal of a WC particle by cavitation erosion. For the BHS-b coatings, almost no large crater is observed. The cross-sectional SEM image (Fig. 6d) also shows that the eutectic Ni-WC networks may impede crack propagation during cavitation erosion. In addition, statistics for the depth of the cavitation craters are also given in Fig. 6e–f (according to the 2D contours given in Fig. S14). The BHS-b coating did not exhibit any deep cavitation craters, suggesting its better resistance to cavitation erosion than the other materials.

In addition, it is also worth mentioning that the BHS-a and BHS-c coatings also exhibited remarkable cavitation erosion resistance, but not as good as the BHS-b coating (Fig. S13, Table S3 and, Table S4). For the BHS-a coating, this could be attributed to the thinner BHS network and sudden detachment of the unmelted WC particles (Fig. S7a1). For the BHS-c coating, the pre-existing pores may compromise its resistance to cavitation erosion (Fig. S7c1).

3.4. *Numerical modelling of the nacre-like hierarchical structure*

The nacre-like sandwiched nanostructure of the eutectic Ni-WC may contribute to the enhanced resistance to cavitation erosion (our testing showed that abalone nacre exhibited good cavitation erosion resistance in Fig. S15). Furthermore, as literature reported that the nanostructure of nacre can effectively dissipate energy [52], we suppose the nacre-like

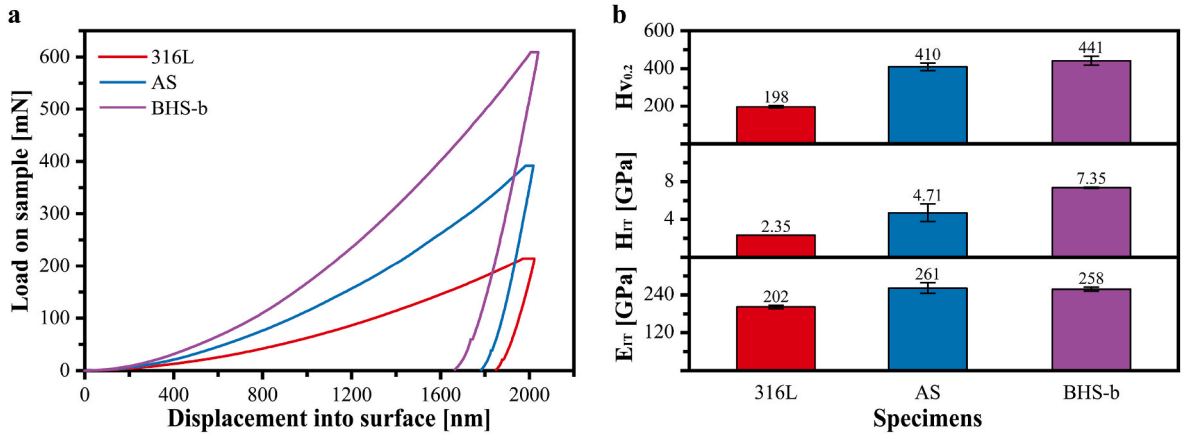

Fig. 4. Mechanical properties of the samples. **a**, Load-displacement plot of the samples indented by a Berkovich diamond indenter. **b**, Vickers hardness under a maximum load of 0.2 kgf ($Hv_{0.2}$), indentation hardness (H_{IT}), and indentation modulus (E_{IT}) of the samples.

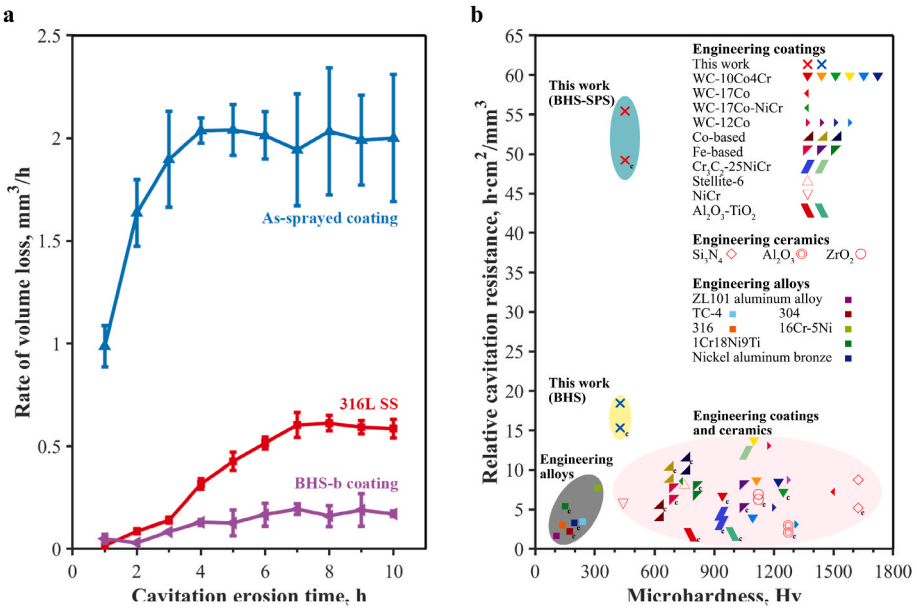

Fig. 5. Cavitation erosion performance of the specimens.
a, Rate of volume loss of the as-sprayed coating, the BHS-b coating, and the 316L SS substrate during cavitation erosion. **b**, Benchmarking against other common engineering materials. The reference materials include engineering coatings (NiCr [32], WC-17Co [32], WC-17Co-NiCr [32], WC-10Co4Cr [30,31,33,36], Cr_3C_2–25NiCr [37], Co-based [38], WC-12Co [36,39], Cr_3C_2–NiCr [36], Al_2O_3–13%TiO_2 [40,41], Fe-based [42], and Stellite-6 [43]), engineering ceramics (Al_2O_3, Si_3N_4, and ZrO_2 [35]), and engineering alloys (Nickel aluminum bronze [8], 316 [30], 304 [31], ZL101 aluminum alloy [32], TC-4 [32], 1Cr18Ni9Ti [33], and 16Cr–5Ni [34]). The subfix 'c' is for those evaluated in corrosive medium.

nanostructure proposed in this work may dissipate the energy from the microjets and shock waves generated by the implosion of cavitation bubbles.

To further gain insight into the nacre-like sandwiched nanostructure, the stress evolution of pure Ni structure and Ni-WC sandwiched structure is extracted and shown in Fig. 7a (a detailed demonstration is given in Fig. S16, Movie S1, and Movie S2), in which only a quarter of the structures are given by considering the symmetry. The compressive stress dominated the stress change in both pure Ni and Ni-WC structures at 0–40 ps, and the tensile stress appears due to the transverse inertia effects at 45 ps. An interesting phenomenon is that the tensile stress is relatively small in the Ni-WC structure as compared to the pure Ni, which can be explained by the relatively large elastic modulus and high density of WC as well as the reduced tensile stress of the structure caused by transverse inertia effects [32]. The failure of elements occurred in both pure Ni and Ni-WC structures at 45–100 ps, which can be recognized as the failure of the elements of the upper surface caused by compressive stress and failure of the elements of the inner structure caused by tensile stress-induced spallation event [32,53]. Regarding the number of failure elements, the pure Ni structure exhibited more failure elements than the Ni-WC structure at 50–70 ps. This explains the inhibition of crack growth at the Ni-WC eutectic network and mitigation of spallation at the Ni-WC interfaces. Furthermore, the tensile stress in the Ni-WC structure is distinctly lower than that in the pure Ni structure at 60 ps, implying that such a sandwiched structure dissipates energy efficiently. There is only little compressive stress in the Ni-WC structure at 70 ps. The tensile stress in the Ni-WC structure reaches the equilibrium state at 100 ps, while relatively high tensile stress remains in the pure Ni structure. It is noteworthy that spallation occurred in both the pure Ni and the Ni-WC sandwich structures at 50 ps. The spall event is located 20–160 nm below the upper surface of the pure Ni structure, whereas it is in 20–100 nm of the Ni-WC sandwich structure.

Supplementary video related to this article can be found at https://doi.org/10.1016/j.compositesb.2022.109730

The stress change of the pure Ni structure and the sandwiched Ni-WC structure along the Z-direction is shown in Fig. 7b. With the depth increase from 50 nm to 400 nm, the tensile stress amplitude in the sandwiched Ni-WC structure is significantly lower than that in the pure Ni structure. The reason likely lies in the multiple interfaces in the sandwiched structure, which contributes to the reflection and the overlapping of stress waves for enhanced energy dissipation efficiently. The change of energy dissipation in the pure Ni structure and the

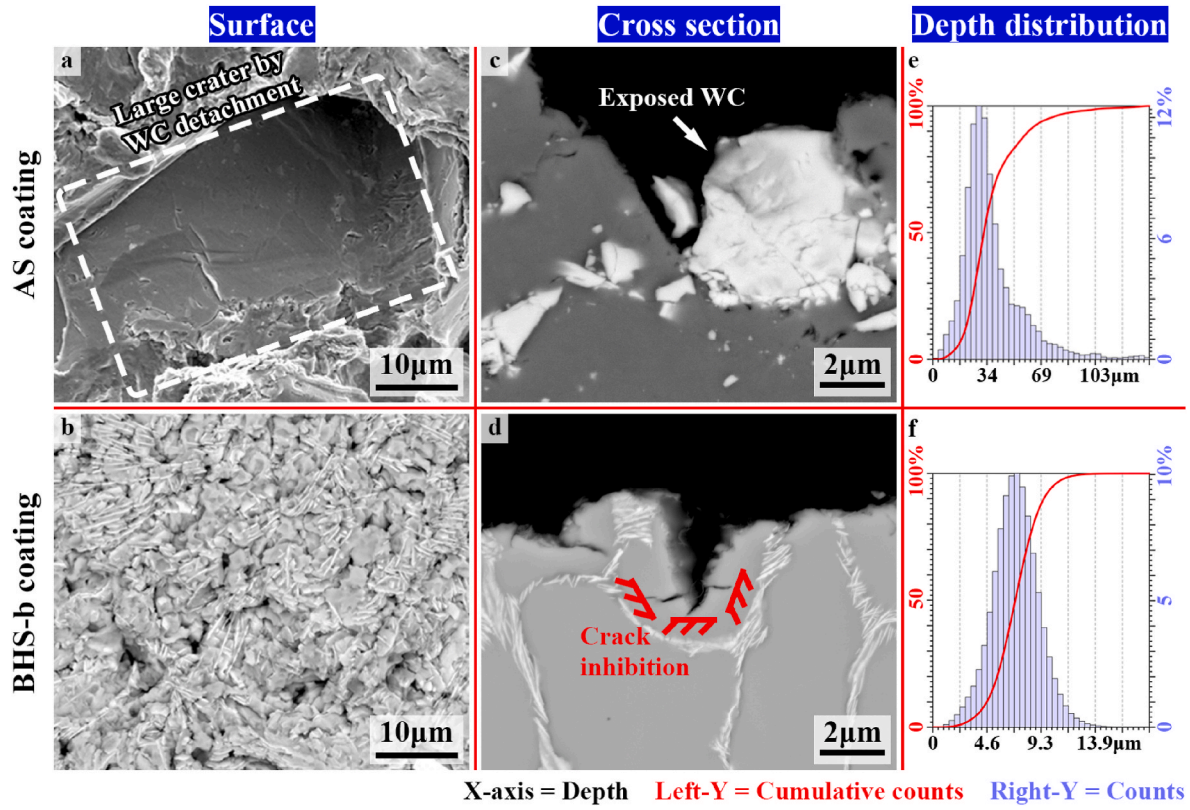

Fig. 6. SEM images and the depth distribution plots for the as-sprayed and the BHS-b coatings subjected to cavitation erosion for 10 h. a-b, SEM images of the eroded cross-sections of the coatings. **c-d**, SEM images of the eroded surfaces of the coatings. **e-f**, the depth distribution on the eroded surface of the coatings according to the 2D contours given in Fig. S14.

sandwiched Ni-WC structure is shown in Fig. 7c. It is noted that the dissipated energy of the sandwiched Ni-WC structure is larger than that of the pure Ni structure at 200 ps. In the Ni-WC structure, Ni accounts for 78.6% of the total mass, while its internal energy is 2.1% higher than the pure Ni structure. The kinetic energy of the whole structure is only 63.5% of the pure Ni structure at 200 ps, which indicates that each WC layer would add two more energy-dissipating interfaces in the sandwiched Ni-WC structure and each interface would facilitate energy dissipation. A schematic diagram showing the failure mechanism of pure Ni structure and the Ni-WC sandwiched structure is presented in Fig. 7d.

4. Discussion

The cavitation erosion resistance of the BHS coatings greatly exceeds that of the AS coating (Fig. 5a), but the improvement of the mechanical properties of the BHS coatings is not that much (Fig. 4). In addition, the BHS coatings exhibit much lower microhardness than the other common engineering coatings but surprisingly show much better resistance to cavitation erosion (Fig. 5b). These indicate that other factors are contributing to the excellent cavitation erosion resistance of the BHS coatings, such as microstructure, which also highly relates to the cavitation erosion behaviour of materials [54,55]. Thus, we attribute the excellent cavitation erosion resistance of the BHS coatings to the improved cohesion of phase boundaries, the particles to lamellar shape transformation of WC grains, and the unique BHS providing damage control and energy dissipation during cavitation erosion.

As shown in Fig. 6a&c, the AS coating exhibits sudden detachment of large WC particles from the Ni binder, leaving craters on the surface during cavitation erosion. This is because the bonding between metal matrix and ceramic particles is mainly mechanical interlocking for the cold-sprayed coating [56,57]. Thus, the ceramic particles could be easily detached from the cold-sprayed cermet coating when subjected to cavitation erosion. In addition, the sudden detachment of large WC particles also results in a large sudden volume loss, which explains the huge fluctuation of $\dot{V}_{loss}$ and V_{loss} of the as-sprayed coating during cavitation erosion (Fig. 5a, Table S3 and Table S4). However, such sudden detachment did not happen for the BHS coatings (Fig. 6b&d), which is likely attributed to the enhanced interface bonding between the precipitated WC grains and the Ni matrix. As opposed to the mechanical interlocking of the cold-sprayed coatings, the SEM and STEM images (Figs. 2a and 3b) clearly show that WC grains are closely bound to the surrounding Ni matrix, resulting in improved cohesive phase boundaries between Ni and WC. Furthermore, the SEM images of the indented surfaces of the coatings (Fig. S9) show microcracks on the indented AS coatings at the interfaces of the Ni-WC boundaries and within the Ni matrix, but no microcracks on the BHS coatings were observed, indicating enhanced boundary bonding by the laser-remelting. It is also worth mentioning that the formation of the complexions (Figs. 2d and Fig. 3c–d) at the phase boundaries during liquid-phase sintering of WC might improve wetting of WC by the liquid metal binder, providing an increased interface strength [34].

Apart from the strengthened Ni-WC interfaces, such remarkable improvement of cavitation erosion may also be attributed to the shape transformation of WC from particles to lamellas and the unique BHS. For the as-sprayed coating, the protection on the Ni matrix provided by the cover of WC particles is limited due to the large area uncovered. For the BHS coatings, the precipitated WC grains are lamellae, and these groups of WC lamella completely wrapped and enclosed the Ni, offering sufficient protection against cavitation erosion. Furthermore, the Ni-WC networks form a cuttlebone-like cellular microstructure, which provides a damage control effect. As shown in Fig. 6d, it is suggested that such cuttlebone-like cellular microstructure can inhibit crack propagation and constrain the crack to be within an individual unit. Compared with the surface of the AS coating, the surface of the BHS coating is much

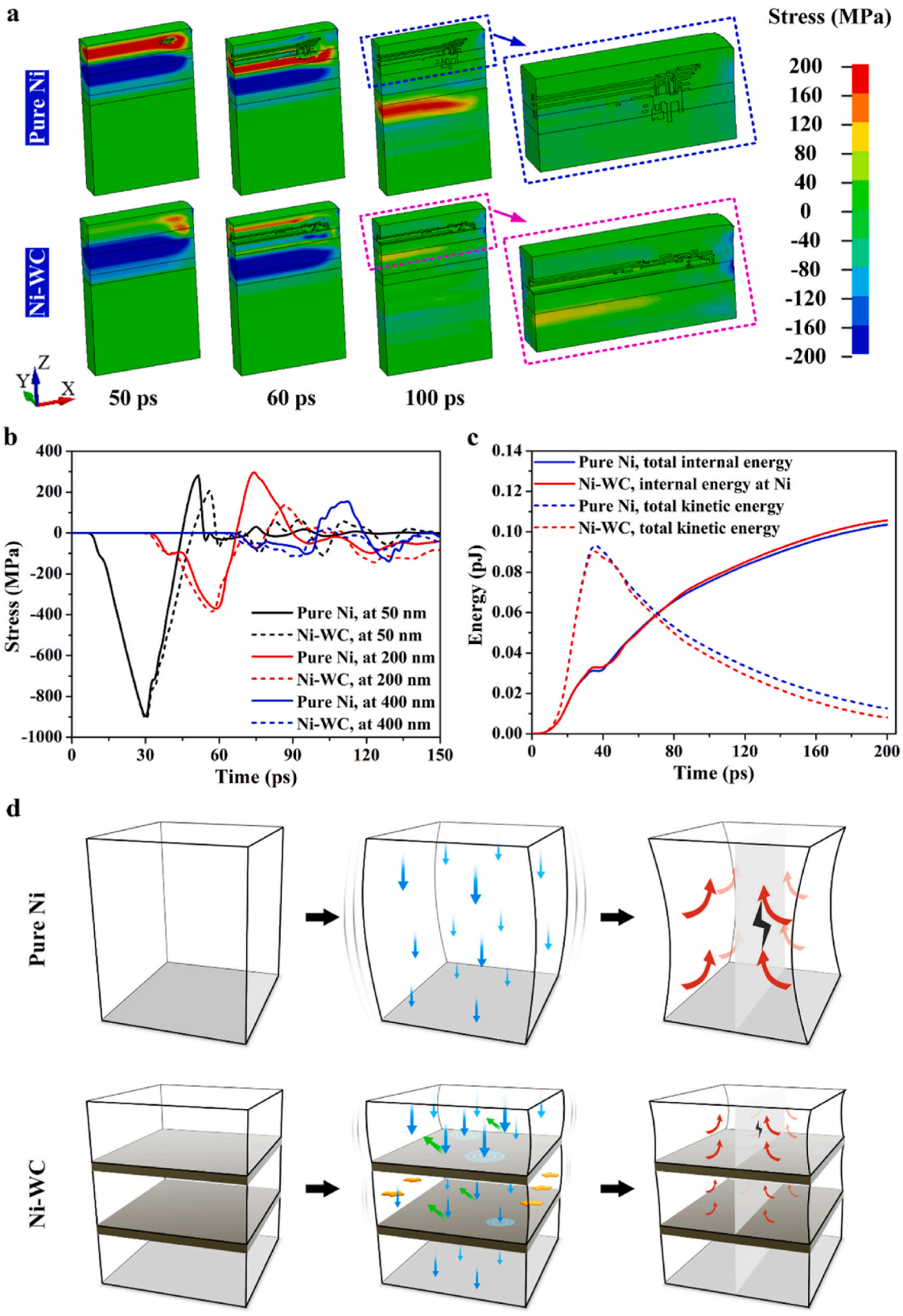

Fig. 7. Cavitation erosion resistant mechanism of the constructed sandwich structure. a, Stress evolution of the pure Ni structure and the Ni-WC sandwich structure when subjected to a triangular shock wave. **b**, Stress change of the pure Ni structure and the Ni-WC sandwich structure along with different Z-direction positions. **c**, Energy change of the pure Ni structure and Ni-WC sandwich structure. **d**, Schematic illustration showing the extraordinary cavitation impact resistance dominated by the bioinspired design. The Ni-WC sandwich structure serves as an impact inhibitor between adjacent Ni grains, facilitating excellent cavitation impact resistance by reducing the tensile stress and improving the energy dissipation capacity, consequently giving rise to the ultrahigh cavitation erosion resistance.

smoother after exposure to cavitation erosion for 10 h (Fig. S14). The depth of the cavitation craters of the BHS-b coating is only ~8 μm, while that of the as-sprayed coating is ~90 μm. Moreover, the statistical analysis of the depth of cavitation craters (Fig. 6f and Fig. S13b3-d3) also shows that the BHS coatings do not exhibit any deep cavitation crater. These have suggested that the eutectic Ni-WC network in the BHS coatings can effectively inhibit the growth of the cracks, providing damage control to the coatings during cavitation erosion. Meanwhile, the precipitated WC grains strongly bind to the Ni matrix, and their newly formed lamellae interlock with the Ni matrix, in turn benefiting the inhibition of crack propagation.

The numerical modelling results further support the hypothesis that the nacre-like sandwiched Ni-WC structure can facilitate the cavitation erosion resistance, and the mechanism is depicted in Fig. 7d. The nacre-like sandwiched Ni-WC structure between adjacent Ni grains could effectively reduce the tensile stress. Thus, both the transverse inertia effect and the reflection and overlapping of stress waves play together. Consequently, the depth of spallation is reduced. In addition, such a sandwiched structure provides more interfaces to promote reflection of the stress waves, thereby improving the energy dissipation capacity for remarkable cavitation erosion resistance.

5. Conclusion

In summary, inspired by the microstructures of the cuttlebone and the abalone nacre, a new bio-mimic hierarchical Ni-WC structure was designed and constructed by laser-remelting treatment of pre-deposited Ni-WC composites. The coatings with bio-mimic hierarchical structure exhibited remarkable resistance to cavitation erosion. The best BHS coating showed the resistance to cavitation erosion with up to 27-fold improvement in the relative cavitation erosion resistance (R_c) compared with common engineering alloys. Such remarkable cavitation erosion resistance is ascribed to the inhibition of crack propagation by the designed network of sandwiched Ni-WC structure, the improvement of bonding strength at phase boundaries, and the lamellar WC grains interlocked with Ni matrix. Furthermore, numerical modelling results revealed that the sandwiched Ni-WC structure could effectively reduce the tensile stress and improve the energy dissipation capacity of the coating when subjected to a burst of cavitation bubble. The improvement is attributed to the transverse inertia effect, reflection, and overlapping of stress waves. Our findings emphasize the relevance of the bio-mimic hierarchical structure to the designing of advanced cavitation erosion resistant materials and provide new insight into the ways of achieving ultrahigh cavitation erosion resistance. Apart from cavitation erosion resistance, we envisage the possibility of promoting the development of a range of other cermet coatings and bulk materials with similar structures for various applications.

Author statement

Ye Tian: Methodology, Investigation, Writing-original draft, Writing-review & editing. Rui Yang: Methodology, Investigation, Writing-original draft, Writing-review & editing. Zhoupeng Gu: Methodology, Investigation, Writing-original draft, Writing-review & editing. Hang Zhao: Methodology, Investigation. Xianqian Wu: Methodology, Writing-review & editing. Shahed Taghian Dehaghani: Methodology, Writing-review & editing. Hao Chen: Writing-review & editing. Xiaomei Liu: Writing-review & editing. Tonghu Xiao: Writing-review & editing. André McDonald: Writing-review & editing. Hua Li: Writing-review & editing. Xiuyong Chen: Conceptualization, Supervision, Writing-original draft, Writing-review & editing.

Data and materials availability

All data are available in the main text or the supplementary materials.

Declaration of competing interest

The authors declare that they have no known competing financial interests or personal relationships that could have appeared to influence the work reported in this paper.

Acknowledgments

The authors would like to thank Mr. Weiqiang Zhu for his assistance in laser-remelting at the University of Nottingham and Ms. Rongrong Jiang, Ms. Yirong Yao, and Ms. Chunting Wang for their assistance in EBSD characterisation and nanoindentation test at Ningbo Institute of Materials Technology and Engineering, Chinese Academy of Sciences. This work was supported by the Zhejiang Provincial Natural Science Foundation of China (grant # LZ22E090001), Ningbo 3315 Talents Program (grant # 2020A-29-G), Chinese Academy of Sciences President's International Fellowship Initiative (grant # 2020VEA0005), National Natural Science Foundation of China (grant # 11672315, 11772347, 21705158 and 51901107), and Natural Sciences and Engineering Research Council of Canada Discovery Grant (grant # NSERC RGPIN-2018-04298).

Appendix A. Supplementary data

Supplementary data to this article can be found online at https://doi.org/10.1016/j.compositesb.2022.109730.

References

[1] Ting RY. Polymer effects on microjet impact and cavitation erosion. Nature 1976;262(5569):572–3.
[2] Sreedhar BK, Albert SK, Pandit AB. Cavitation damage: theory and measurements – a review. Wear 2017;372–373:177–96.
[3] Long X, Cheng H, Ji B, Arndt REA, Peng X. Large eddy simulation and Euler–Lagrangian coupling investigation of the transient cavitating turbulent flow around a twisted hydrofoil. Int J Multiphas Flow 2018;100:41–56.
[4] Shojaei P, Trabia M, O'Toole B, Jennings R, Zhang X, Liao Y. Enhancing hypervelocity impact resistance of titanium substrate using Ti/SiC metal matrix nanocomposite coating. Compos B Eng 2020;194:108068.
[5] Peng Y, Wang H, Zhao C, Hu H, Liu X, Song X. Nanocrystalline WC-Co composite with ultrahigh hardness and toughness. Compos B Eng 2020;197:108161.
[6] Hong S, Wu YP, Zhang JF, Zheng YG, Qin YJ, Lin JR. Ultrasonic cavitation erosion of high-velocity oxygen-fuel (HVOF) sprayed near-nanostructured WC-10Co-4Cr coating in NaCl solution. Ultrason Sonochem 2015;26:87–92.
[7] Tzanakis I, Eskin DG, Georgoulas A, Fytanidis DK. Incubation pit analysis and calculation of the hydrodynamic impact pressure from the implosion of an acoustic cavitation bubble. Ultrason Sonochem 2014;21(2):866–78.
[8] Ye L, Zhu X, He Y, Wei X. Ultrasonic cavitation damage characteristics of materials and a prediction model of cavitation impact load based on size effect. Ultrason Sonochem 2020;66:105115.
[9] Cottam R, Luzin V, Moody H, Edwards D, Majumdar A, Wong YC, et al. The role of microstructural characteristics in the cavitation erosion behaviour of laser melted and laser processed Nickel–Aluminium Bronze. Wear 2014;317(1–2):56–63.
[10] Zhang LM, Ma AL, Yu H, Umoh AJ, Zheng YG. Correlation of microstructure with cavitation erosion behaviour of a nickel-aluminum bronze in simulated seawater. Tribol Int 2019;136:250–8.
[11] Hardes C, Pohl F, Rottger A, Thiele M, Theisen W, Esen C. Cavitation erosion resistance of 316L austenitic steel processed by selective laser melting (SLM). Addit Manuf 2019;29:10.
[12] Wang Y, Liu J, Kang N, Darut G, Poirier T, Stella J, et al. Cavitation erosion of plasma-sprayed CoMoCrSi coatings. Tribol Int 2016;102:429–35.
[13] Kwok CT, Man HC, Cheng FT, Lo KH. Developments in laser-based surface engineering processes: with particular reference to protection against cavitation erosion. Surf Coating Technol 2016;291:189–204.
[14] Cadman J, Zhou SW, Chen YH, Li W, Appleyard R, Li Q. Characterization of cuttlebone for a biomimetic design of cellular structures. Acta Mech Sin 2010;26(1):27–35.
[15] Cadman J, Zhou SW, Chen YH, Li Q. Cuttlebone: characterisation, application and development of biomimetic materials. J Bionic Eng 2012;9(3):367–76.
[16] Mao AR, Zhao NF, Liang YH, Bai H. Mechanically efficient cellular materials inspired by cuttlebone. Adv Mater 2021;33(15):2007348.
[17] Wegst UG, Bai H, Saiz E, Tomsia AP, Ritchie RO. Bioinspired structural materials. Nat Mater 2015;14(1):23–36.
[18] Sun J, Bhushan B. Hierarchical structure and mechanical properties of nacre: a review. RSC Adv 2012;2:7617–32.

[19] Verho T, Karppinen P, Groschel AH, Ikkala O. Imaging inelastic fracture processes in biomimetic nanocomposites and nacre by laser speckle for better toughness. Adv Sci 2018;5(1):1700635.
[20] Traxel KD, Bandyopadhyay A. Naturally architected microstructures in structural materials via additive manufacturing. Addit Manuf 2020;34:101243.
[21] Radi K, Jauffres D, Deville S, Martin CL. Strength and toughness trade-off optimization of nacre-like ceramic composites. Compos B Eng 2020;183:107699.
[22] Tan G, Zhang J, Zheng L, Jiao D, Liu Z, Zhang Z, et al. Nature-inspired nacre-like composites combining human tooth-matching elasticity and hardness with exceptional damage tolerance. Adv Mater 2019;31(52):e1904603.
[23] Magrini T, Bouville F, Lauria A, Le Ferrand H, Niebel TP, Studart AR. Transparent and tough bulk composites inspired by nacre. Nat Commun 2019;10(1):2794.
[24] Grossman M, Pivovarov D, Bouville F, Dransfeld C, Masania K, Studart AR. Hierarchical toughening of nacre-like composites. Adv Funct Mater 2019;29(9):1806800.
[25] Yin Z, Hannard F, Barthelat F. Impact-resistant nacre-like transparent materials. Science 2019;364(6447):1260–3.
[26] Song YH, Wu KJ, Zhang TW, Lu LL, Guan Y, Zhou F, et al. A nacre-inspired separator coating for impact-tolerant lithium batteries. Adv Mater 2019;31:1905711.
[27] Zhan JM, Yao XH, Zhang XQ. Shock response of metal-ceramic nanolayered composites. Compos B Eng 2020;199:108272.
[28] Wan H, Leung N, Algharaibeh S, Sui T, Liu Q, Peng H-X, et al. Cost-effective fabrication of bio-inspired nacre-like composite materials with high strength and toughness. Compos B Eng 2020;202:108414.
[29] Melendez NM, McDonald AG. Development of WC-based metal matrix composite coatings using low-pressure cold gas dynamic spraying. Surf Coating Technol 2013;214:101–9.
[30] Zhang HJ, Gong YF, Chen XY, McDonald A, Li H. A comparative study of cavitation erosion resistance of several HVOF-sprayed coatings in deionized water and artificial seawater. J Therm Spray Technol 2019;28(5):1060–71.
[31] Gu ZP, Wu XQ, Li QM, Yin QY, Huang CG. Dynamic compressive behaviour of sandwich panels with lattice truss core filled by shear thickening fluid. Int J Impact Eng 2020;143:103616.
[32] Yu Y, Chen D, Tan H, Wang H, Xie S, Zhang M. Spall investigations for LY12 Al using triangular waves. Int J Impact Eng 2007;34:395–404.
[33] Liu XX, Song X, Wang H, Liu XX, Tang F, Lu H. Complexions in WC-Co cemented carbides. Acta Mater 2018;149:164–78.
[34] Konyashin I, Sologubenko A, Weirich T, Ries B. Complexion at WC-Co grain boundaries of cemented carbides. Mater Lett 2017;187:7–10.
[35] Wang Q, Tang Z, Cha L. Cavitation and sand slurry erosion resistances of WC-10Co-4Cr coatings. J Mater Eng Perform 2015;24(6):2435–43.
[36] Ding X, Huang Y, Yuan C, Ding Z. Deposition and cavitation erosion behavior of multimodal WC-10Co4Cr coatings sprayed by HVOF. Surf Coating Technol 2020;392:125757.
[37] Hou G, Zhao X, Zhou H, Lu J, An Y, Chen J, et al. Cavitation erosion of several oxy-fuel sprayed coatings tested in deionized water and artificial seawater. Wear 2014;311(1–2):81–92.
[38] Hong S, Wu Y, Zhang J, Zheng Y, Qin Y, Lin J. Ultrasonic cavitation erosion of high-velocity oxygen-fuel (HVOF) sprayed near-nanostructured WC-10Co-4Cr coating in NaCl solution. Ultrason Sonochem 2015;26:87–92.
[39] Kumar RK, Seetharamu S, Kamaraj M. Quantitative evaluation of 3D surface roughness parameters during cavitation exposure of 16Cr-5Ni hydro turbine steel. Wear 2014;320:16–24.
[40] Niebuhr D. Cavitation erosion behavior of ceramics in aqueous solutions. Wear 2007;263(1–6):295–300.
[41] Liu J, Chen T, Yuan C, Bai X. Performance analysis of cavitation erosion resistance and corrosion behavior of HVOF-sprayed WC-10Co-4Cr, WC-12Co, and Cr_3C_2-NiCr coatings. J Therm Spray Technol 2020;29(4):798–810.
[42] Mayer AR, Bertuol K, Siqueira I, Chicoski A, Vaz RF, de Sousa MJ, et al. Evaluation of cavitation/corrosion synergy of the Cr_3C_2-25NiCr coating deposited by HVOF process. Ultrason Sonochem 2020;69:105271.
[43] Hou G, Ren Y, Zhang X, Dong F, An Y, Zhao X, et al. Cavitation erosion mechanisms in Co-based coatings exposed to seawater. Ultrason Sonochem 2020;60:104799.
[44] Du J, Zhang J, Zhang C. Effect of heat treatment on the cavitation erosion performance of WC-12Co coatings. Coatings 2019;9(10):690.
[45] Deng W, Hou G, Li S, Han J, Zhao X, Liu X, et al. A new methodology to prepare ceramic-organic composite coatings with good cavitation erosion resistance. Ultrason Sonochem 2018;44:115–9.
[46] Deng W, An Y, Zhao X, Zhang C, Tang L, Liu J. Cavitation erosion behavior of ceramic/organic coatings exposed to artificial seawater. Surf Coating Technol 2020;399:126133.
[47] Zheng ZB, Zheng YG, Sun WH, Wang JQ. Effect of heat treatment on the structure, cavitation erosion and erosion-corrosion behavior of Fe-based amorphous coatings. Tribol Int 2015;90:393–403.
[48] Lavigne S, Pougoum F, Savoie S, Martinu L, Klemberg Sapieha JE, Schulz R. Cavitation erosion behavior of HVOF CaviTec coatings. Wear 2017;386–387:90–8.
[49] Sreedhar BK, Albert SK, Pandit AB. Improving cavitation erosion resistance of austenitic stainless steel in liquid sodium by hardfacing – comparison of Ni and Co based deposits. Wear 2015;342–343:92–9.
[50] Song QN, Tong Y, Xu N, Sun SY, Li HL, Bao YF, et al. Synergistic effect between cavitation erosion and corrosion for various copper alloys in sulphide-containing 3.5% NaCl solutions. Wear 2020;450:203258.
[51] Gao G, Zhang Z. Cavitation erosion behavior of 316L stainless steel. Tribol Lett 2019;67(4):112.
[52] Huang ZW, Pan ZL, Li HZ, Wei QM, Li XD. Hidden energy dissipation mechanism in nacre. J Mater Res 2014;29(14):1573–8.
[53] Kanel GI. Spall fracture: methodological aspects, mechanisms and governing factors. Int J Fract 2010;163:173–91.
[54] Chiu KY, Cheng FT, Man HC. Cavitation erosion resistance of AISI 316L stainless steel laser surface-modified with NiTi. Mater Sci Eng, A 2005;392(1–2):348–58.
[55] Lima MM, Godoy C, Modenesi PJ, Avelar-Batista JC, Davison A, Matthews A. Coating fracture toughness determined by Vickers indentation: an important parameter in cavitation erosion resistance of WC-Co thermally sprayed coatings. Surf Coating Technol 2004;177:489–96.
[56] Lienhard J, Crook C, Azar MZ, Hassani M, Mumm DR, Veysset D, et al. Surface oxide and hydroxide effects on aluminum microparticle impact bonding. Acta Mater 2020;197:28–39.
[57] Assadi H, Kreye H, Gärtner F, Klassen T. Cold spraying – a materials perspective. Acta Mater 2016;116:382–407.